Draft version January 21, 2022
Typeset using LaTeX **twocolumn** style in AASTeX63

arXiv:1911.02834v1 [astro-ph.HE] 7 Nov 2019

MULTIWAVELENGTH VARIABILITY SIGNATURES OF RELATIVISTIC SHOCKS IN BLAZAR JETS

Markus Böttcher[1] and Matthew G. Baring[2]

[1] *Centre for Space Research, North-West University, Potchefstroom, 2531, South Africa*
[2] *Department of Physics and Astronomy - MS 108, Rice University, 6100 Main Street, Houston, Texas 77251-1892, USA*

ABSTRACT

Mildly-relativistic shocks that are embedded in colliding magnetohydrodynamic flows are prime sites for relativistic particle acceleration and production of strongly variable, polarized multi-wavelength emission from relativistic jet sources such as blazars and gamma-ray bursts. The principal energization mechanisms at these shocks are diffusive shock acceleration and shock drift acceleration. In recent work, we had self-consistently coupled shock acceleration and radiation transfer simulations in blazar jets in a basic one-zone scenario. These one-zone models revealed that the observed spectral energy distributions (SEDs) of blazars strongly constrain the nature of the shock layer hydromagnetic turbulence. In this paper, we expand our previous work by including full time dependence and treating two zones, one being the site of acceleration, and the second being a larger emission zone. This construction is applied to multiwavelength flares of the flat spectrum radio quasar 3C 279, fitting snap-shot SEDs and generating light curves that are consistent with observed variability timescales. We also present a generic study for the typical flaring behavior of the BL Lac object Mrk 501. The model predicts correlated variability across all wavebands, but cross-band time lags depending on the type of blazar (FSRQ vs. BL Lac), as well as distinctive spectral hysteresis patterns in all wavelength bands, from *mm* radio waves to gamma-rays. These evolutionary signatures serve to provide diagnostics on the competition between acceleration and radiative cooling.

Keywords: Acceleration of particles — plasmas — shock waves — turbulence — galaxies: active — galaxies: jets — X-rays — gamma-rays

1. INTRODUCTION

Extragalactic jets of active galactic nuclei (AGN) and gamma-ray bursts (GRBs) are some of the most powerful emitters of radiation in the Universe, identifying them as sites of efficient particle acceleration. Relativistic, oblique, magnetohydrodynamic (MHD) shocks internal to these jets have long been considered as one of the leading contenders for the sites of relativistic particle acceleration that seeds the observed rapidly variable, often highly-polarized multi-wavelength (MW) emission. The dominant particle acceleration mechanisms at such shocks are diffusive shock acceleration (DSA) and shock drift acceleration (SDA), inextricably linked and often collectively referred to as first-order Fermi acceleration.

In DSA, particle energization results from repeated shock crossings of particles. For this process to be effective, the particles's gyrational motion along large-scale ordered magnetic fields has to be reversed by some process. In the case of DSA, this reversal of particle momenta $\mathbf{p}$ along magnetic field lines is facilitated by diffusive pitch-angle scatterings (PAS) in strong, chaotic MHD turbulence. Note that many such pitch angle scatterings arise per gyroperiod, and their accumulation generates diffusive mean free paths that are usually fairly close to (but exceed) a charge's gyroradius – see Summerlin & Baring (2012) for details. It is also possible that larger angle scatterings can contribute, an element that forms the focus of the blazar/shock acceleration study in Stecker et al. (2007).

In SDA, the gradient in the electric field across the shock discontinuity does work on charges and accelerates them promptly and in episodes of gyrational reflection off the shock layer, interspersed with upstream diffusive excursions by the particles in which they are forced to return to the shock by the dominant convective flow (Decker, & Vlahos 1986; Summerlin & Baring 2012). In contrast to DSA, for shock drift energization

Markus.Bottcher@nwu.ac.za

baring@rice.edu

to be at its most effective, the MHD turbulence level has to be relatively low, so that reflections in the shock layer are not disrupted, and the net diffusive mean free path far exceeds the gyroradius. Accordingly, DSA and SDA complement each other in terms of their acceleration capability, respectively dominating when the field turbulence is strong (DSA) near the shock discontinuity, or the field is substantially more laminar on much larger spatial scales (SDA). This picture of a concentration of MHD turbulence nearer the shock is represented in Fig. 2 of BBS17.

We remark that the concept of SDA is dependent on the frame of reference. In the de Hoffman Teller (HT) shock rest frame, where the flow velocity $\mathbf{u}$ and magnetic field $\mathbf{B}$ vectors are parallel to each other both upstream and downstream ($\mathbf{u} \times \mathbf{B} = \mathbf{0}$), there is no large-scale electric field and, thus, no SDA. If one views the shock in the so-called normal incidence frame (NIF), which is obtained via a particular Lorentz boost $\mathbf{v}$ in the plane of the shock, the upstream flow velocity $\mathbf{u}$ is normal to the shock plane and a large-scale $\mathbf{v} \times \mathbf{B}$ electric field exists in the NIF, thereby facilitating an identifiable SDA. For an extensive discourse on the relationship between plasma turbulence, charge transport and acceleration by the DSA and SDA processes, the reader may consult Summerlin & Baring (2012) and Baring, Böttcher & Summerlin (2017).

Theoretical studies of particle acceleration at relativistic shocks (e.g., Kirk & Heavens 1989; Ellison, Jones & Reynolds 1990; Ellison & Double 2004; Summerlin & Baring 2012) have shown that the shock acceleration process can result in a wide variety of spectral indices for the particle distribution, up to a limiting slope of $n(p) \propto p^{-s}$ with $s = 1$. In particular, Summerlin & Baring (2012) highlight the fact that flat $s \sim 1$ power laws develop when turbulence is low and SDA dominates the acceleration process, as charges are effectively trapped for long periods in or upstream of the shock layer. These circumstances contrast the steeper distributions with $s \sim 2.5$ that emerge from particle-in-cell (PIC) kinetic plasma simulations where the Weibel instability enhances the turbulence that drives the acceleration process (e.g., Sironi & Spitkovsky 2009; Sironi, Spitkovsky & Arons 2013), but diminishes the trapping of charges near the shock layer. Similar indices $s \sim 2.2$ are observed for electrons in PIC simulations of the current-driven Bell instability at mildly-relativistic shocks (Crumley et al. 2019). The reader can consult Marcowith et al. (2016) for a comprehensive review of the microphysics of shock acceleration. Note that magnetic reconnection models can also develop distributions with $s \sim 1 - 1.5$ (e.g. Cerutti, Uzdensky & Begelman 2012), though PIC simulations of charge transport between X-point locales for energization and moving magnetic islands indicate a steepening of the acceleration distribution index to $s \sim 1.5 - 4$, depending on the plasma magnetization (Sironi, & Spitkovsky 2014).

Such studies of particle acceleration usually do not consider the resulting radiative signatures in a self-consistent manner, and clearly observational constraints on s and other byproducts of acceleration theory would be extremely insightful. On the other hand, models focusing on the time-dependent, multi-zone radiative transfer problem for internal-shock models of blazars (e.g., Marscher & Gear 1985; Spada et al. 2001; Sokolov, Marscher & McHardy 2004; Mimica et al. 2004; Sokolov & Marscher 2005; Graff et al. 2008; Böttcher & Dermer 2010; Joshi & Böttcher 2011; Chen et al. 2011, 2012) typically approximate the results of shock acceleration by assuming an ad-hoc injection of purely non-thermal relativistic particles, usually with a broken and/or truncated power-law distribution in energy. Therefore, blending these two aspects of the jet dissipation problem to enable deeper insights is strongly motivated.

To this end, in recent work (Baring, Böttcher & Summerlin 2017, hereafter BBS17), we coupled the Monte Carlo (MC) simulations of shock acceleration from Summerlin & Baring (2012) with the steady-state radiative transfer routines of Böttcher et al. (2013). This provided, for the first time, a consistent description of the separate but intertwined mechanisms of DSA and SDA and their radiative signatures in mildly relativistic, oblique shocks in blazar jets. An integral element of such an approach is that it includes complete distributions of leptonic populations of non-thermal plus thermal particles, thereby enabling observational constraints on the values of important jet plasma quantities such as the lepton number density n_e, and consequently the electron plasma frequency $\omega_{\rm p} = [4\pi n_e e^2/m_e]^{1/2}$ and the magnetization $\Sigma = \sigma/\gamma = B^2/[\,4\pi n_e m_e c^2\,]$. Fits to the spectral energy distributions (SEDs) of three blazars indicated the need for a strongly energy-dependent PAS diffusive mean-free path $\lambda_{\rm pas} \propto p^{\alpha}$, with $\alpha \sim 2$ – 3, depending on the type of blazar. This may be considered as evidence of hydromagnetic turbulence levels gradually decreasing with increasing distance from the shock (BBS17), and the dominance of SDA for electrons at energies exceeding ~ 30 MeV.

In this work, we present an extension of the shock acceleration + radiation-transfer model of BBS17, including full time variability. We make predictions for time-dependent snap-shot SEDs, and produce MW light

curves, which can be further analyzed to predict multi-wavelength spectral hysteresis patterns and inter-band time lags. A brief summary of our model and its application to a gamma-ray flare of the Flat Spectrum Radio Quasar (FSRQ) 3C 279 in late 2013 and early 2014, which exhibited a negligible change of the Compton dominance compared to the quiescent state, was outlined in Böttcher & Baring (2019). Here we present the full model description, and apply our model to another flare of 3C 279 which is part of the same active phase of this blazar in the 2013 – 2014 epoch, but exhibits a greatly increased Compton dominance, as is more typical of the multi-wavelength flaring behaviour of FSRQs. Additionally, we detail two case studies for the BL Lac object Mrk 501. These are not applied to any specific flaring episodes, such as the stunning VHE variability on timescales of a few minutes reported in Albert et al. (2007), but rather to a generic description of the collection of flares garnered in MW campaigns for Mrk 501 over the last two decades.

In Section 2, we describe our model setup and the numerical scheme we developed for simulating combined time-dependent shock acceleration and radiation transfer in internal shocks in blazars. Results of the application of our numerical scheme to two well-known γ-ray blazars are presented in Section 3. Specifically, we model two contrasting multi-wavelength flares of the FSRQ 3C 279 (Section 3.1), one with an extreme increase of the Compton dominance, yielding good MW spectral fits and distinctive temporal characteristics illustrated using hardness-intensity diagrams and discrete correlation functions. An obvious strength of our 3C 279 modeling is that it simultaneously describes *both* the multi-wavelength spectroscopy and the variability patterns. We further present in Section 3.2 template models of typical multi-wavelength flaring behaviour of the high-frequency-peaked BL Lac object (HBL) Mrk 501, with predictions of expected spectral variability behavior. Specifically, we model two test cases: one in which the flaring is caused only by a change of the total power of particles accelerated due to shock acceleration, and one representing the characteristic extreme synchrotron peak shift to higher frequencies often observed in Mrk 501 during flaring states, requiring a significant change of the mean free path for pitch-angle scattering of shock-accelerated particles. We summarize and discuss our results in Section 4. Throughout the manuscript, unprimed symbols denote quantities in the emission-region (jet) rest frame, while a superscript '$*$' refers to quantities in the AGN rest frame and a superscript 'obs' signifies the observer's frame.

2. MODEL SETUP AND NUMERICAL SCHEME

The plasma in relativistic jets of AGN is known to propagate at bulk speeds $\beta^*_\Gamma c$ corresponding to bulk Lorentz factors $\Gamma^* \sim 5 - 40$ (e.g., Dondi & Ghisellini 1995; Jorstad et al. 2005). In the case of blazars, these jets are oriented at a small angle $\theta^*_{\rm obs} \lesssim 1/\Gamma^*$ to our line of sight, resulting in strong Doppler boosting of the emission by a Doppler factor of $\delta = 1/\sqrt{1-\beta^*_\Gamma\,\cos\theta^*_{\rm obs}} \sim \Gamma^*$ in observed frequency and a factor of δ^4 in observed bolometric flux, compared to quantities measured in the co-moving frame of the jet plasma.

Our underlying assumption throughout this work is that mildly relativistic shocks with jet frame Lorentz factors $\Gamma_{\rm s} \sim 1-3$ propagate through the jets of blazars at all times, leading to time-variable diffusive shock acceleration in small acceleration zones proximate to shock fronts. These modest $\Gamma_{\rm s}$ shocks naturally arise when two ultra-relativistic MHD flows collide. A quiescent state is established through a balance between continuous and steady particle energization in the acceleration zone, and radiative cooling and escape of particles in a larger radiation zone of length $\ell_{\rm rad}$ (measured in the co-moving frame of the jet material), which is identified with the high-energy emission region (see BBS17 and Figure 2 therein for details). Enhanced emission and variability arises from the passage of a mildly relativistic shock through the density and magnetic field structures in the high-energy emission region, on an observed time scale $\Delta t_{\rm obs} = (\ell_{\rm rad}/v_{\rm s})\,(1+z)/\delta$. Here $v_{\rm s}$ is the shock velocity in the co-moving frame of the jet material and z is the cosmological redshift of the source. Turbulence on larger scales that may well seed such shock structures is routinely generated in both hydrodynamic and MHD simulations (e.g., Meliani et al. 2008; Porth 2013; Barniol Duran, Tchekhovskoy & Giannios 2017).

In the conventional shock acceleration scenario, the first-order Fermi acceleration process that includes episodes of shock drift energization is facilitated by stochastic pitch angle diffusion of charges spiraling along magnetic field lines. A useful parameterization of the mean-free path for pitch angle scattering is $\lambda_{\rm pas} = \eta(p)\,r_{\rm g}$, i.e. via a momentum-dependent multiple $\eta(p)$ of the particle's gyro radius, $r_{\rm g} = pc/(qB)$, where p is the particle's momentum. A broadly applicable choice for the scaling is a power-law in the particle's momentum, $\eta(p) = \eta_1\,(p/mc)^{\alpha-1}$, where η_1 describes the mean free path in the non-relativistic limit, $\gamma \to 1$. Motivations for this form from hybrid plasma simulations, quasi-linear MHD turbulence theory and *in-situ* spacecraft observations in the he-

liosphere are discussed in Summerlin & Baring (2012); Baring, Böttcher & Summerlin (2017).

For the acceleration/injection pipeline of our MW modeling here, an array of representative thermal plus non-thermal particle distributions resulting from DSA+SDA for various values of the shock speed v_s, magnetic-field obliquity Θ_{Bf1}, and PAS mean-free-path parameters η_1 and α have been generated using the Monte Carlo code of Summerlin & Baring (2012), with some examples being displayed in Fig. 1 of BBS17. This ensemble of MC simulations illustrates that shock acceleration leads to a non-thermal broken power-law tail of relativistic particles which have been accelerated out of the remaining thermal pool. As a consequence of the $\eta(p) \propto p^{\alpha-1}$ form, the particle distribution is somewhat steep ($dn/dp \sim p^{-2.2}$) at low momenta when DSA dominates, and much flatter ($dn/dp \sim p^{-1}$) for much higher momenta when SDA is the more effective energization process. We note that these distributions are somewhat anisotropic in the shock rest frame (which moves at a mildly-relativistic speed relative to the jet frame) due to the strong convective action in relativistic shocks – e.g., see Figs. 4 and 5 in Summerlin & Baring (2012).

A high-energy cut-off at Lorentz factor $\gamma_{max} \approx p_{max}/m_e c$ of the non-thermal particle spectra results from the balance of the acceleration time scale $t_{acc}(\gamma_{max}) = \eta(\gamma_{max})\, t_g(\gamma_{max})$ with the radiative energy loss time scale. If synchrotron losses dominate, $\gamma_{max} \propto B^{-1/2}$. This will lead to a synchrotron peak energy $E_{syn} \sim 240\,\delta/[\,\eta(\gamma_{max})\,]$ MeV. Notably, this synchrotron peak energy is independent of the magnetic field B, as $E_{syn} \propto B\,\gamma_{max}^2$. Blazars typically show synchrotron peaks in the IR to soft X-rays. In order to reproduce these, the pitch angle scattering mean-free-path parameter $\eta(\gamma_{max})$ has to assume values of $\sim 10^4$ – 10^8, first noted by Inoue & Takahara (1996). However, Summerlin & Baring (2012) have shown that η_1 must be significantly smaller than this $\eta(\gamma_{max})$ value in order to obtain efficient injection of particles out of the thermal pool into the non-thermal acceleration process. From these arguments one can infer that $\eta(p)$ must be strongly dependent on momentum p (BBS17).

The shock acceleration-generated thermal + non-thermal electron spectra serve as a particle injection term into simulations of subsequent radiative cooling of the electrons. To keep the number of parameter variations to a minimum, as in BBS17, here we will adopt a shock speed of $v_s = 0.71c$, a magnetic field obliquity to the shock normal of $\Theta_{Bf1} = 32.3°$, an upstream gas temperature of 5.45×10^7 K, and a velocity compression ratio of $r = 3.71$. These choices well represent the environment of a strong, subluminal, mildly-relativistic shock. Summerlin & Baring (2012) note that there is modest sensitivity of the accelerated electron distributions to the magnetic obliquity Θ_{Bf1}, and also that changes in the electron temperature will alter the velocity compression ratio across the shock, and the distributions somewhat. Yet the objective of this paper is to identify the key acceleration characteristics that are required to successfully model time-dependent, MW blazar spectra in a two-zone construct. Accordingly, focusing on a fairly representative shock set up suffices for these goals, and an extensive exploration of spectral model variations with shock parameters is deferred to future work.

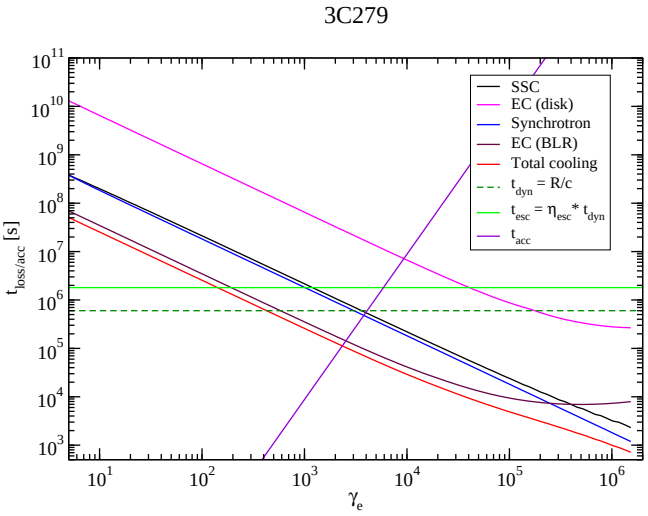


Figure 1. The relevant timescales as functions of electron Lorentz factor in the simulated quiescent-state equilibrium configuration for 3C 279, i.e. the green spectrum in Figure 2 (see Section 3.1 for details). The diagonal curves/lines represent the acceleration time (purple), radiative cooling (black, pink, blue, brown, red — see legend), and the horizontal lines are the dynamical (green dashed) and escape (light green solid) timescales.

As relevant radiative mechanisms, synchrotron radiation in a tangled magnetic field, synchrotron self-Compton (SSC) radiation, and inverse Compton scattering of external radiation fields (external inverse Compton = EIC) on various plausible target photon fields are taken into account in our simulations. All the relevant cooling rates, emissivities, and absorption coefficients are evaluated using the routines described in detail in Böttcher et al. (2013). Particles may also leave the emission region on a time scale parameterized as a multiple of the light-crossing time scale of the emission region, $t_{esc,e} = \eta_{esc}\,\ell_{rad}/c$. Thus, $\sqrt{\eta_{esc}}\,\ell_{rad}$ approximately represents (for $\eta_{esc} \gg 1$) the diffusive mean free path in long wavelength MHD turbulence in the radia-

tion zone, with values far exceeding the short, gyro-scale pathlengths encountered by low energy charges undergoing DSA within the confines of the very turbulent shock layer.

Figure 1 shows the energy dependence of the relevant time scales for the steady state generated to describe the quiescent-state multi-wavelength emission of 3C 279 (see Section 3.1). DSA+SDA will be effective up to an energy $\gamma_{\rm max}$, where the radiative cooling time scale becomes shorter than the acceleration time scale. Figure 1 illustrates that for almost all particles at lower energies, $\gamma < \gamma_{\rm max}$, the acceleration time scale is many orders of magnitude shorter than the radiative cooling and/or escape timescales. This implies that for particles of all energies significantly below $\gamma_{\rm max}$, the DSA process acts effectively instantaneously, while radiative cooling or escape are negligible. Thus, numerically, DSA may be well represented as an instantaneous injection of relativistic particles at a (time-dependent) rate $Q_e(\gamma_e, t)$ [cm^{-3} s^{-1}], which is then followed by evolution on the radiative and escape time scales in the larger emission zone. For our 3C 279 case study, $\gamma_{\rm max} \sim (2-3)\times 10^3$. For Mrk 501, it is substantially higher at $\gamma_{\rm max} \sim 4\times 10^5$, similar to the values derived in BBS17.

The injection function $Q_e(\gamma_e, t)$ is the distribution computed in the MC simulation, folded with an exponential cutoff of the form $\exp(-\gamma/\gamma_{\rm max})$. The normalization of the injection function $Q_e(\gamma_e, t)$ is determined through an injection luminosity, $L_{\rm inj}$ (in the co-moving jet frame), as

$$L_{\rm inj} = \frac{4\pi}{3}\,\ell_{\rm rad}^3\, m_e c^2 \int_1^\infty Q_e(\gamma_e, t)\,\gamma_e\, d\gamma_e \quad . \qquad (1)$$

A simplification adopted in this first exploration of time-dependent radiation signatures of relativistic shocks in AGN jets, is that we assume that the shock conditions and diffusion parameters (η_1, α) remain constant during the passage of the shock (injection), and separately constant also during the quiescent phases before and after the shock passage. Accordingly $Q_e(\gamma, t)$ involves a simple Heaviside step function in time, with the shock passage lasting a mere few hours. This simplification of the shock evolution is a first approximation, noting that the only observational constraints on changing shock conditions are based on the flux variability on the observed variability timescale, and this timescale is captured in our model prescription. We defer the study of a more realistic and self-consistent time dependence of pitch-angle diffusion parameters and the resulting $Q_e(\gamma, t)$ to future work.

The distribution of relativistic electrons is assumed to be isotropic in the co-moving frame of the emission region, and its evolution is simulated by numerically solving a Fokker-Planck equation of the form

$$\frac{\partial n_e(\gamma_e, t)}{\partial t} = -\frac{\partial}{\partial \gamma_e}\Big(\dot\gamma_e\, n_e[\gamma_e, t]\Big) - \frac{n_e(\gamma_e, t)}{t_{\rm esc,e}} + Q_e(\gamma_e, t)\,. \qquad (2)$$

The solution is obtained using an implicit Crank-Nicholson scheme as described in Böttcher & Chiang (2002). In Eq. (2), $\dot\gamma_e$ represents the combined radiative energy loss rate of the electrons, and all quantities are in the co-moving frame of the emission region, and the electron escape time scale is parameterized as a multiple of the light-crossing time scale, $t_{\rm esc,e} = \eta_{\rm esc}\, R/c$.

Radiation transfer is handled by forward evolution of a continuity equation for the photons,

$$\frac{\partial n_{\rm ph}(\epsilon, t)}{\partial t} = \frac{4\,\pi\, j_\epsilon}{\epsilon\, m_e c^2} - c\,\kappa_\epsilon\, n_{\rm ph}(\epsilon, t) - \frac{n_{\rm ph}(\epsilon, t)}{t_{\rm esc,ph}}\,. \qquad (3)$$

Here j_ϵ and κ_ϵ are the emissivity and absorption coefficient, respectively, $\epsilon = h\nu/(m_e c^2)$ is the dimensionless photon energy, and $t_{\rm esc,ph}$ is the photon escape time scale, $t_{\rm esc,ph} = (4/3)\,\ell_{\rm rad}/c$ for a spherical geometry (Böttcher et al. 1997). Because of the tangled magnetic field assumed in the radiation zone, the synchrotron photons that seed the SSC signal are presumed isotropic. In contrast, the external radiation field that is upscattered to form the EIC component is assumed to be isotropic in the AGN rest frame, as appropriate for the BLR or dust torus radiation fields, as long as these seed photons are emitted within the BLR radius or the dust torus, respectively. Accordingly, this field is Doppler-boosted and highly anisotropic in the jet frame, thereby strongly enhancing the EIC emissivity. The total observed flux from the synchrotron, SSC and EIC emission is provided by the escaping photons, such that

$$\nu F_\nu^{\rm obs}(\nu_{\rm obs}, t_{\rm obs}) = \frac{\epsilon^2\, m_e c^2\, n_{\rm ph}(\epsilon, t)\,\delta^4\, V_{\rm rad}}{4\pi\, d_L^2\,(1+z)\, t_{\rm esc,ph}} \quad , \qquad (4)$$

where $\epsilon = (1+z)\epsilon_{\rm obs}/\delta$ and $V_{\rm rad} \approx (4/3)\,\pi\,\ell_{\rm rad}^3$ is the co-moving volume of the emission region. The jet-frame and observer time intervals are related through $\Delta t_{\rm obs} = \Delta t\,(1+z)/\delta$. Our code outputs snap-shot SEDs and multi-wavelength light curves at 7 pre-specified frequencies ν_i. For the present work, we chose ν_i as listed in Table 1. All radiation spectra are corrected for $\gamma\gamma$ absorption by the Extragalactic Background Light (EBL) using the model of Finke, Razzaque & Dermer (2010). However, for the test cases discussed below, the effect of EBL absorption is small (particularly for 3C 279 with little flare emission above 10 GeV) and has no effect on the resulting light curve or cross-correlation features.

For the purpose of producing hardness-intensity diagrams, our code also extracts local spectral indices at

Table 1. Observed frequencies for which light curves and local spectral indices are extracted in our simulations.

No.	Frequency	Band	Blazar
$\nu_1^{\rm obs}$	230 GHz	Radio	3C 279
$\nu_2^{\rm obs}$	5.5×10^{14} Hz	Optical R-band	3C 279, Mrk 501
$\nu_3^{\rm obs}$	2.4×10^{17} Hz	1 keV X-rays	3C 279, Mrk 501
$\nu_4^{\rm obs}$	2.4×10^{18} Hz	10 keV X-rays	Mrk 501
$\nu_5^{\rm obs}$	2.4×10^{19} Hz	100 keV X-rays	Mrk 501
$\nu_6^{\rm obs}$	2.4×10^{23} Hz	1 GeV γ-rays	3C 279, Mrk 501
$\nu_7^{\rm obs}$	2.4×10^{26} Hz	1 TeV γ-rays	3C 279, Mrk 501

the frequencies ν_i for each time step. Correlations between the light curves at different frequencies and possible inter-band time lags τ are evaluated using the Discrete Correlation Function (DCF) analysis as detailed in (Edelson & Krolik 1988). This is a discretization of the correlation function

$$\mathcal{C}_{a,b}(\tau) \equiv \frac{1}{\mathcal{N}_a\mathcal{N}_b}\int_{-T}^{T} F_a^{\rm obs}(t)\,F_b^{\rm obs}(\tau-t)\,dt \qquad (5)$$

which accounts for errors due to uneven sampling. Here, fluxes $F_{a,b}^{\rm obs}$ are in wavebands a,b, with

$$\mathcal{N}_a = \int_{-T}^{T} F_a^{\rm obs}(t)\,dt \qquad (6)$$

defining the normalizations, and the times τ and t being implicitly in the observer frame. The bracketing time T is chosen large enough that the solutions realize the long-term quiescent state. As will become evident in due course, the lags τ will be tightly coupled to the relative cooling times in different wavebands.

For each flare simulation, we first let the radiation code run until it reaches a stable equilibrium with a set of quiescent-state parameters. An individual flaring event is then simulated by changing various input parameters as a function of time. The default mode for such changes will be a step function in time for the duration $\Delta t = \ell_{\rm rad}/v_{\rm s}$ in the co-moving frame of the emission region. The value of the shock speed $v_{\rm s}$ in the jet frame is that used in the Monte-Carlo acceleration code to simulate the electron injection spectra; this is fixed at the representative value of $v_{\rm s} = 0.71c$.

3. RESULTS

The code described in the previous section has been applied to two test cases: (1) Two multi-wavelength flares of the FSRQ 3C 279 during the active period in 2013 - 2014 (Hayashida et al. 2015), and (2) a generic test case for the typical SED and variability patterns of the prototypical HBL Mrk 501 (e.g., Abdo et al. 2011; Ahnen et al. 2018). These present contrasting examples that evince a range of spectral and temporal character.

3.1. *Application to 3C 279*

The FSRQ 3C 279, located at a redshift of $z = 0.536$ (Lynds et al. 1965), gained prominence due to its exceptional gamma-ray activity during the early days of the Energetic Gamma-Ray Experiment Telescope (EGRET) on board the *Compton* Gamma-Ray Observatory (CGRO) in the early 1990s (e.g, Wehrle et al. 1998; Hartman et al. 2001). It continues to be one of the brightest gamma-ray blazars detected by the Large Area Telescope (LAT) on board the *Fermi* Gamma-Ray Space Telescope (e.g., Abdo et al. 2010a), and is one of only a handful of FSRQs also detected in very-high-energy (VHE: $E > 100$ GeV) gamma rays by ground-based Imaging Atmospheric Čerenkov Telescopes (IACTs; e.g., Teshima et al. 2008; De Naurois 2018).

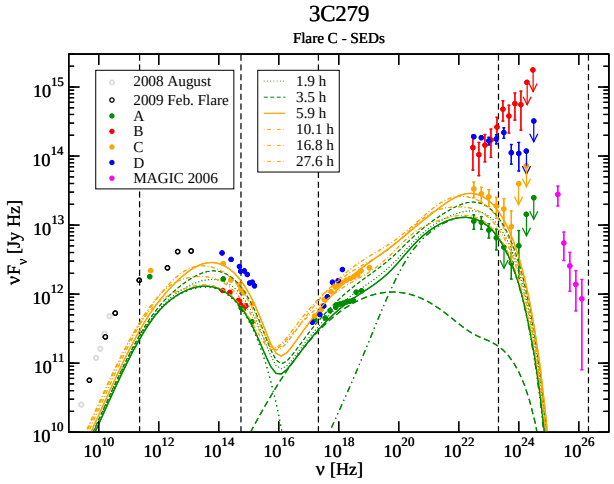


Figure 2. Snap-shot SEDs of 3C 279 during 2013 – 2014, with a model simulation to reproduce Flare C. Data are from Hayashida et al. (2015). The heavy solid green curves show the quiescent-state (period A) fit, with individual radiation components shown as dotted (synchrotron), dashed (SSC) and dot-dot-dashed (EIC on dust torus photons) curves. Light green curves illustrate the spectral evolution during the rising part of the simulated Flare C; yellow curves show the evolution during the decaying part. The dashed vertical lines indicate the frequencies at which light curves and hardness-intensity diagrams are extracted (see Table 1).

Extensive multi-wavelength observations of 3C 279 during flaring activity in the period December 2013 – April 2014 were reported in Hayashida et al. (2015). Figure 7 of that paper shows multi-wavelength light

curves of 3C 279, where several γ-ray flares (B, C, D) are identified, in addition to a quiescent period (A). Figure 2 shows snap-shot SEDs extracted by Hayashida et al. (2015) for these episodes, along with our model simulation to reproduce Flare C. The quiescent state (period A) has been reproduced with the model parameters listed in Table 2. The characteristic time scale of short-term flares of 3C 279 during the 2013 – 2014 period (including Flare C) is $\Delta t^{\rm obs} \sim 0.3 - 1$ day. Throughout this paper, we assume a viewing angle of $\theta^*_{\rm obs} \approx 1/\Gamma^*$, and a typical Doppler factor of $\delta \approx \Gamma^* = 15$, a value that satisfies pair compactness lower bounds of $\delta \gtrsim 8 - 10$ for 3C 279 as discussed in Maraschi, Ghisellini & Celotti (1992) and Ghisellini et al. (1993). Then, for this δ and given the redshift of $z = 0.536$, for a mildly relativistic shock with $v_{\rm s} \sim 0.7c$, the variability timescale implies a size of the active region of $\ell_{\rm rad} \sim 1.8 \times 10^{16}$ cm.

Table 2. Model parameters for the fit to 3C-279 SEDs during the quiescent-state (period A).

Parameter	Value
Jet-frame parameters	
Electron injection luminosity	$L_{\rm inj,q} = 1.1 \times 10^{43}$ erg s^{-1}
Emission region size	$\ell_{\rm rad} = 1.8 \times 10^{16}$ cm
Jet-frame magnetic field	$B = 0.65$ G
Escape time scale parameter	$\eta_{\rm esc} = 3$
Thermal e^+e^- density	$n_e = 1.2 \times 10^4$ cm^{-3}
PAS m.f.p. low-energy limit	$\eta_1 = 100$
PAS m.f.p. scaling index	$\alpha = 3$
AGN-frame parameters	
Bulk Lorentz factor	$\Gamma^* = \delta = 15$
Accretion-disk luminosity	$L^*_d = 6 \times 10^{45}$ erg s^{-1}
Distance from BH	$z^*_i = 0.1$ pc
Ext. rad. field energy density	$u^*_{\rm ext} = 4 \times 10^{-4}$ erg cm^{-3}
Ext. rad. field BB temperature	$T^*_{\rm ext} = 300$ K.

We find that, to model the quiescent-state SED of 3C 279, EIC needs to be dominated by scattering of a low-temperature external radiation field, as expected to arise from the dusty torus. For the present study, we approximate it as a thermal blackbody at a temperature of $T^*_{\rm ext} = 300$ K. The quiescent state fit is illustrated by the solid green line in Fig. 2. We find that it can be well described with an electron injection spectrum produced by DSA+SDA with a pitch-angle scattering mean free path scaling as $\lambda_{\rm pas} = 100\, r_g\, (p/m_e c)^2$, i.e., $\lambda_{\rm pas} \propto p^3$. Based on the competition of acceleration and cooling time scales, as illustrated in Fig. 1, electrons are accelerated up to a maximum energy of $\gamma_{\rm max} = 2.4 \times 10^3$. In the quiescent-state equilibrium, the magnetization of the emission region is $u_B/u_e = 0.094$, which satisfies the requirement of a weakly magnetized medium for the formation of a strong shock. Note that u_B/u_e relates to the non-relativistic magnetization Σ as listed in Table 3 via $u_B/u_e = \Sigma/(2\langle\gamma_e\rangle)$, where $\langle\gamma_e\rangle$ is the average (relativistic) electron Lorentz factor.

We point out that many of the emission-region parameter values are degenerate in the sense that they depend on the assumed value of the bulk Lorentz factor Γ^* and the Doppler factor δ, which have been assigned typical values for this source. However, within reasonable bounds on Γ^* and δ, the general conclusions concerning the plasma physics and turbulence characteristics will not change. In particular, we emphasize that the location of the synchrotron peak (modulo the Doppler factor) closely constrains the value of $\lambda_{\rm pas}(\gamma_{\rm max})$, as it is independent of the magnetic field. This leaves a degeneracy between η_1 and α, which would change primarily the thermal-to-non-thermal particle density ratio, but not significantly alter the radiative signatures. As in BBS17, there is an approximate tolerance of about ± 0.2 in α, and a tolerance of a factor of $\sim 1 - 5$ in η_1 permitting MW spectral fits of similar character and precision.

3.1.1. *3C 279 — Flare C*

For the study of expected multi-wavelength variability in the internal-shock model, we first focus on Flare C (yellow in Figure 2), which is characterized by an almost unchanged Compton dominance compared to the quiescent state during period A. One natural interpretation is that this and other flares closely sample the accelerator/injector (e.g., Yan, Zhang & Zhang 2016). Therefore, such flaring behaviour can plausibly be reproduced by merely increasing the number of radiating non-thermal electrons generated by the shock, thus enhancing the synchrotron and EIC emission at the same rate. Specifically, in our simulation, after reaching a steady state with the input parameters listed in Table 2, we increase the electron injection luminosity to $L_{\rm inj,f} = 5.0 \times 10^{43}$ erg s^{-1}, i.e., about 4.5 times its value $L_{\rm inj,q}$ during the quiescent state. All parameter changes for the flaring episodes C and B (see Section 3.1.2) are summarized in Table 3. To identify more intimately the changes in physical conditions in the jet, those listed include the derived parameters of the cyclotron frequency, $\omega_{\rm B}$, the thermal electron number density n_e at the end of the flare injection episode, the

plasma frequency, $\omega_{\rm p}$ and the non-relativistic magnetization, $\Sigma = B^2/[\,4\pi n_e m_e c^2\,] \equiv \omega_{\rm B}^2/\omega_{\rm p}^2$.

Table 3. Parameters adopted to reproduce the quiescent state and flares C and B of 3C 279. All values are in the jet frame.

Parameter†	Quiescent	Flare C Dec. 31, 2013	Flare B Dec. 20, 2013
$L_{\rm inj}$ [erg s^{-1}]	1.1×10^{43}	5.0×10^{43}	4.0×10^{44}
B [G]	0.65	0.65	0.075*
η_1	100	100	10
α	3	3	2.3
n_e [cm^{-3}]	1.2×10^{4}	2.23×10^{4}	2.15×10^{4}
$\omega_{\rm B}$ [MHz]	11.4	11.4	1.32
$\omega_{\rm p}$ [MHz]	6.18	8.42	8.27
$\Sigma = \omega_{\rm B}^2/\omega_{\rm p}^2$	3.42	1.84	0.025

Note: † The cyclotron frequency $\omega_{\rm B}$, the electron number density n_e, the plasma frequency $\omega_{\rm p}$ and magnetization Σ are values derived using B and $L_{\rm inj}$. *This field is at the outset of an exponential recovery, described in Eq. (7), i.e. B_f therein.

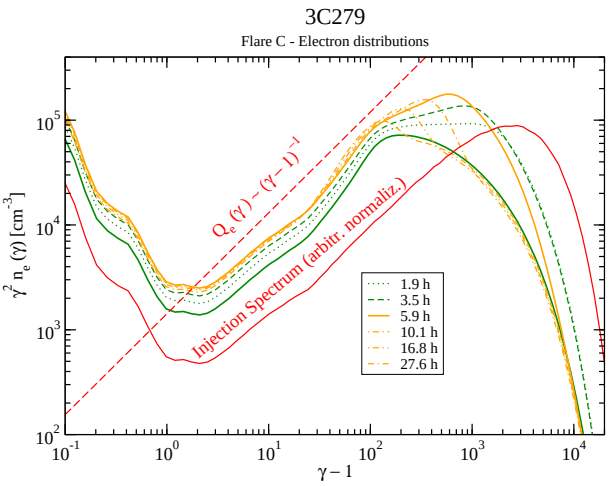


Figure 3. Electron distribution sequence $n_e(\gamma_e, t)$ corresponding to the Flare C simulation illustrated in Fig. 2. The diagonal line marks the approximate shock injection power law distribution that results primarily from the shock drift (SDA) mechanism: see Summerlin & Baring (2012), BBS17.

Snap-shot SEDs during various times of the spectral evolution of this Flare C simulation are shown by the light curves in Figure 2, with light green curves illustrating the rising portion, and light yellow curves illustrating the decaying phase of the flare. The heavy yellow curve shows the SED during the peak of the flare. The excellent fit to both the period A and C SEDs indicates that such variability can be produced without any changes of the turbulence and particle acceleration characteristics, as long as a 4.5-fold increase in the injection luminosity $L_{\rm inj}$ of accelerated electrons can be achieved. We note that this amplification factor differs from the factor of 1.86 enhancement in the density n_e of the thermal electron population (see Table 3), because of the influences of cooling and escape on the electron distribution function: see Eq. (2). The evolution of the electron distribution throughout the Flare C sequence is depicted in Figure 3, clearly illustrating the competition between acceleration and cooling at the highest Lorentz factors.

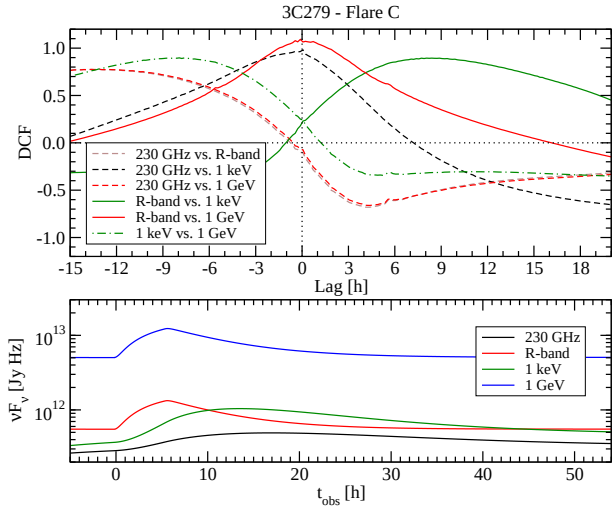


Figure 4. *Bottom:* Multi-wavelength light curves extracted from the Flare C simulation illustrated in Fig. 2. Injection from shock acceleration starts at $t_{\rm obs} = 0$ and ends at $t_{\rm obs} = 5.5$ hr, after which cooling reduces the R Band and GeV fluxes. *Top:* Discrete cross correlation functions evaluated from the light curves shown in the bottom panel: see Eq. (5) and associated text for details.

The resulting light curves in the *mm* radio, optical, X-ray and GeV γ-ray bands are illustrated in the bottom panel of Fig. 4. Unfortunately, the observational data for Flare C are too sparsely sampled to warrant a detailed comparison between observations and the model light curves. No significant TeV emission is predicted by our simulation, in accordance with the finding by Böttcher et al. (2009) that leptonic models have difficulties reproducing the VHE emission observed in several exceptional flare states of 3C 279. The physical origin of this is in the low value of $\gamma_{\rm max}$, imposed by

the very strong Compton cooling in the emission region, and required to generate the low synchrotron peak frequency. No VHE emission was detected from 3C 279 during the 2013 – 2014 flaring episodes discussed in Hayashida et al. (2015), though there have been detections by IACTs, for example by MAGIC in 2006 which is included as archival VHE flux points (magenta) in Figure 2. Using these light curves, cross-correlations between the various frequency bands can be calculated; these are depicted in the top panel of Fig. 4; see also Teshima et al. (2008).

The model predicts, as expected in most leptonic single-emission-zone models for FSRQs, that the optical and γ-ray light curves are closely correlated with zero time lag, as those bands are produced by synchrotron and Compton emission from electrons of similar energies, sampling electrons with energies near $\gamma_{\rm max}$. They therefore possess comparable cooling times that are short, driving the prompt declines in flux seen in Figure 4 once the injection is terminated. The X-ray emission, being dominated by SSC emission of low-energy electrons with significantly longer cooling time scales than those producing the optical and GeV γ-ray emission, is expected to lag behind the optical and γ-ray emissions by $\sim$ 8 hr, while the *mm* radio band is expected to show an even longer delay behind optical and γ-rays, with slightly weaker correlation. These are manifested in the much slower drops in X-ray and radio fluxes once the shock injection is shut off, occurring on timescales of 15–30 hours. Unfortunately, the light curve coverage in most existing data for 3C 279 is not sufficient for a detailed, direct comparison of our predictions with observations. This includes the radio, optical and X-ray data reported in Hayashida et al. (2015). Yet we observe that our model duration of around 15 hours for the GeV flare signal is very consistent with the duration of Flare C as observed by *Fermi*-LAT. This, combined with the satisfactory spectral reproduction of MW data, instills a confidence in the robustness of the hybrid acceleration-emission modeling approach adopted here.

Figure 5 shows the hardness-intensity diagrams (HIDs) extracted from our simulatons of flare C. The hardness is represented by the spectral index here and for all HIDs presented in the paper, with the index corresponding to the differential energy flux spectrum, i.e. F_ν. While only very weak spectral variability is predicted in the optical and GeV γ-ray bands, pronounced clockwise spectral hysteresis (harder rising-flux spectra; softer decaying-flux spectra) is expected in the *mm* radio and X-ray bands. Due to the typically faint X-ray fluxes from FSRQs (X-rays covering the valley between the synchrotron and Compton spectral components), it is difficult to discern such spectral hysteresis in the X-ray observations of such objects — in contrast to HBLs, where the X-ray emission is synchrotron dominated (e.g., Takahashi et al. 1996). Observing such features in other wavelength bands could enable stringent constraints on the magnetic field and the shock injection in the emission region (see, e.g., Kirk et al. 1998; Böttcher et al. 2003). Yet the predicted spectral hysteresis at optical and GeV energies may be too subtle to be detected by current-generation instrumentation. However, we note that on longer time scales of $\sim 25-30$ days associated with general source variability, the WEBT campaign for 3C 279 detailed in Böttcher et al. (2007) indicates for one time interval a counter-clockwise hysteresis loop in an optical B-R color versus R magnitude HID diagram in Fig. 5 therein, and for a preceding interval, a tilted figure 8 hysteresis profile. Since these are not closely related to shock-instigated flare activity, they provide no insights into our present models.

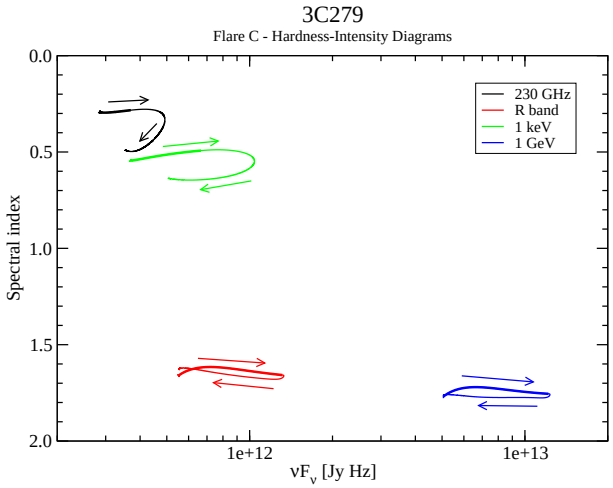


Figure 5. Hardness-intensity diagrams extracted from the Flare C simulation illustrated in Figs. 2 — 4, with the spectral index serving as a proxy for traditional hardness ratios.

3.1.2. *3C279 — Flare B*

Flare C discussed above is somewhat atypical for FSRQ flares as it exhibits a negligible increase in the Compton dominance compared to the quiescent state. A much more common occurrence are variability patterns exhibiting larger flux ranges at higher energies, i.e., strongly increasing Compton dominance during multi-wavelength flares, as is evident during flare B (red SEDs in Figs. 2 and 6). Such flaring behavior can plausibly be explained by a temporary increase of the energy density of the external target photon field for EIC Compton scattering, e.g., in synchrotron mirror scenarios as

proposed by Böttcher & Dermer (1998); Tavani et al. (2015); MacDonald et al. (2015, 2017), which might not require any changes of the particle acceleration process in the emission region. The exploration of such scenarios is outside the scope of this paper, which is to study the effects of time-varying turbulence and particle acceleration characteristics in blazar jets.

In this Subsection, we investigate what changes in magnetohydrodynamic turbulence, particle acceleration and other source-intrinsic parameters would be required in order to reproduce flare B of Hayashida et al. (2015) without invoking a temporary change of the external radiation field. We choose flare B for this exercise, as it appears to present an especially challenging case of an "orphan" γ-ray flare with no significant counterpart in the optical (synchrotron) flux.

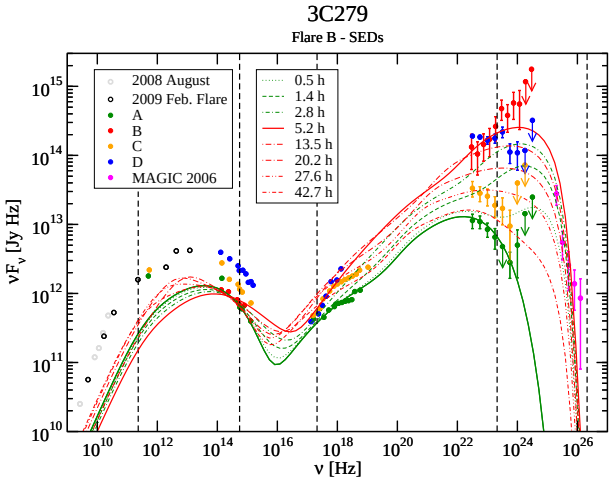


Figure 6. Snap-shot SEDs from the modeling of flare B of 3C 279 in December 2013 (Data from Hayashida et al. 2015). The heavy solid green curves show the quiescent-state (period A) fit. Light green curves illustrate the spectral evolution during the rising part of the simulated Flare B; red curves show the evolution during the decaying part. The dashed vertical lines indicate the frequencies at which light curves and hardness-intensity diagrams are extracted.

The γ-ray spectrum in the Flare B SED is significantly harder than the (episode A) quiescent SED. This requires significantly harder electron injection spectra. The simplest way to achieve this is via a change of the turbulence/diffusion parameters $\eta_1 = 100 \rightarrow 10$ and $\alpha = 3 \rightarrow 2.3$. A good fit to the Flare B γ-ray SED could then be obtained if the electron injection luminosity also changes to $L_{\rm inj,f} = 4.0 \times 10^{44}$ eg/s, i.e., ~ 36 times the quiescent level. If this were the only change in parameters, the model would naturally predict an equally strong flux flaring and spectral hardening in the synchrotron spectrum (especially in the optical), which is not observed. Within our single-radiation-zone model, keeping the optical flux constant during the γ-ray flare requires a reduction of the magnetic field by an amount that exactly compensates for the increased injection of high-energy electrons. We find that with a change of $B = 0.65 \rightarrow 0.075$ G, the optical spectrum will undergo only moderate spectral-index changes, while maintaining its overall flux. The SSC component is also not dramatically modified, thereby avoiding an unobserved overproduction of X rays.

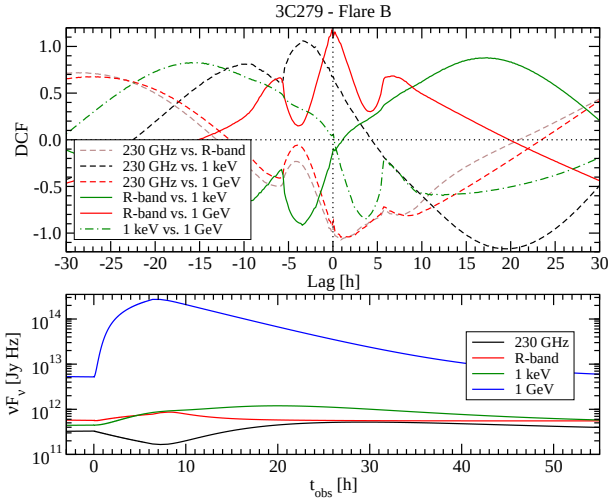


Figure 7. *Bottom:* Multi-wavelength light curves extracted from the Flare B simulation illustrated in Fig. 6. *Top:* Discrete cross correlation functions evaluated from the light curves shown in the bottom panel.

Another issue occurs at the end of the flaring episode (i.e., when the shock causing the flare either leaves the emission region or loses its strength), where our standard model assumption was that all parameters revert to their quiescent-state values. At the end of the flare activation period, this additional injection has built up a significant excess of high-energy electrons, from which it takes several days in the observer's frame to re-establish the quiescent-state electron distribution. Thus, if the magnetic field were to relax to its (higher) quiescent-state value immediately at the end of the flaring injection episode, a large optical flare would result around ~ 1 day subsequent to the γ-ray Flare B, which has not been observed (Hayashida et al. 2015). Suppressing this flare requires that the magnetic field is only gradually restored to its quiescent-state value. A simulation that does not predict significant optical variability could be achieved with a gradual restoration of the magnetic field

of the form

$$B(t) = B_q + (B_f - B_q)\, e^{-(t'-t'_{\rm end})/t'_{\rm rec}} \quad , \quad t' > t'_{\rm end} \ , \quad (7)$$

i.e., after the end of the flare injection episode, $t'_{\rm end}$, on a time scale of $t'_{\rm rec} = 2.8 \times 10^5$ sec (in the co-moving frame). This time scale is of the order of the characteristic radiative cooling time scale of electrons that are emitting optical synchrotron photons when 3C 279 is in its quiescent state, i.e. episode A. Here, B_f is the field at the onset of Flare B, and B_q is the long-term quiescent value as listed in Table 3. In Section 4 we will discuss critically whether such a combined change of parameters could represent a realistic internal-shock scenario in a blazar jet.

Fig. 7 shows, analogous to the case of flare C in the previous sub-section, the multi-wavelength light curves and cross-correlation functions between different wavelength bands. The combination of parameter changes differs from those for Flare C, and the gradual restoration of the magnetic field leads to more complicated variability patterns, especially in the optical, as well as anti-correlated variability (a dip) in the radio light curve compared to all higher frequencies. The origin of the dip in the radio flux is primarily the prompt reduction in the magnetic field at the onset of Flare B, which more than offsets the rise in the non-thermal electron density. Interestingly, the 6-hour rise time of the 1 GeV light curve and its 10–15 hour e-fold decay timescale are fairly consistent with the high time-resolution *Fermi*-LAT data displayed in Fig. 2 of Hayashida et al. (2015).

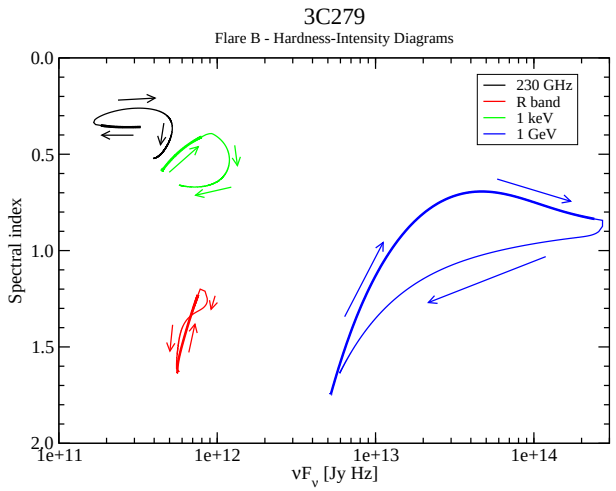


Figure 8. Hardness-intensity diagrams extracted from the Flare B simulation illustrated in Figs. 6 — 7.

What little variability that remains in the optical light curve is expected to be well correlated with the γ-ray light curve, i.e. with zero delay. As in the case of flare C, the X-rays are delayed with respect to the γ-rays and optical emission, but with a significantly longer delay timescale of about $\sim$ 16 hours. This is a direct consequence of the lower magnetic field and, thus, longer radiative cooling time scale of the low-energy electrons responsible for the SSC X-ray emission[1].

The hardness-intensity diagrams plotted in Fig. 8 illustrate that the large-amplitude γ-ray flaring activity during flare B is predicted to be associated with significant clockwise spectral hysteresis (as in flare C, harder spectrum during rising flux, softer during decaying flux), with spectral-index changes on $\sim$ a few hours time scales. Such variations may be measurable with *Fermi*-LAT during the brightest γ-ray flares of 3C 279, as is evidenced by its temporal resolution of Flare B at the 3 hour level (e.g., see Fig. 2 of Hayashida et al. 2015). Significant spectral hysteresis, similar to that predicted for flare C, is also predicted in the X-rays, but their detection may be hampered by the relatively low X-ray flux of FSRQs like 3C 279.

Table 3 lists three derived parameters for Flares B and C that inform the physical process of acceleration. The first of these is the electron gyrofrequency, $\omega_{\rm B}$, which represents the fundamental scale of the Fermi DSA process when it is efficient. It is of the order of a few MHz for our quiescent emission and Flare B and C models. In our implementation, the acceleration rate is $d\gamma/dt \sim \omega_{\rm B}/\eta(p)$ with $\eta(p) \gg 1$ ensuring that the energization rate is much slower than Bohm-limited DSA and SDA drives the acceleration process. The plasma frequency $\omega_{\rm p}$ is of similar order to $\omega_{\rm B}$ in all three models so that the magnetization $\sigma = \omega_{\rm B}^2/\omega_{\rm p}^2$ ranges between 0.02 and 4. Since $c/\omega_{\rm p}$ is the inertial scale in electrodynamic systems, $\omega_{\rm p}$ defines the rate of Wiebel-instability driven acceleration in shocks imbued with strong MHD turbulence, or an approximate scaling for the magnetic reconnection acceleration rate in relativistic systems with multiple sites distributed amid converging magnetic islands – see the discussion in BBS17. Therefore, $\omega_{\rm p} \gg \omega_{\rm B}/\eta(p)$ and from this one infers that acceleration driven by either reconnection or by the Weibel instability in their basic forms is too efficient to accommodate the infrared or optical synchrotron peak in 3C 279. They essentially are too turbulent, as is the Bohm-limited Fermi shock configuration. System modifications that suitably reduce their

[1] Recall that the higher Compton dominance during flare B is achieved by a harder electron spectrum without a change of the external radiation field. Thus, a lower magnetic field will be directly reflected in a longer radiative cooling time scale.

acceleration efficiency are therefore necessary and these are subject to the constraints of time variability, just as for our successful invocation of the SDA process at shocks. This assessment also applies to our subsequent study of Mrk 501, and blazars in general.

3.2. *Application to Mrk 501*

Mrk 501 is one of the archetypal TeV blazars, an HBL at a redshift of $z = 0.034$ (e.g., Grazian et al. 2000), and the second extragalactic source detected in VHE γ-rays by the Whipple Telescope (Quinn et al. 1996; Bradbury et al. 1997). The SED of Mrk 501 is typical of HBLs with the synchrotron peak in the X rays, and the SSC (in our leptonic interpretation) peak located at VHE γ-rays. The synchrotron component often dominates the total bolometric output so that the Compton-dominance parameter is $C \lesssim 1$. The very hard γ-ray spectrum of Mrk 501 was reflected in a non-detection at GeV energies by EGRET, even during VHE γ-ray flaring episodes (Catanese et al. 1997), but the improved sensitivity of *Fermi*-LAT allowed detailed studies of its GeV spectral properties and variability (Abdo et al. 2011). Mrk 501 is one of only a handful of blazars from which VHE γ-ray variability on time scales down to a few minutes has been observed (Albert et al. 2007). Our study here of the expected spectral variability of Mrk 501 in an internal-shock model with consistent particle acceleration generated at shocks is based on the long-term averaged SED compiled by Abdo et al. (2011), see Fig. 9.

The SEDs of HBLs are often successfully reproduced by pure SSC models, requiring no external radiation fields as targets for Compton scattering to produce the γ-ray emission (e.g., Ghisellini et al. 2010), and the same holds true for Mrk 501 (e.g., Petry et al. 2000). A quiescent-state SED fit to Mrk 501 with a steady-state version of our model was already presented in BBS17, and a similar fit with a pure SSC model serves as the starting point for our variability study here. Table 4 lists the parameters used, and we remark that they differ somewhat from those chosen in BBS17, most notably by the adoption here of a higher magnetic-field strength, but a lower electron injection luminosity. A noteworthy difference from the case of 3C 279 is the large escape time scale parameter $\eta_{\rm esc}$ needed for Mrk 501. This is required by the SED data in order to achieve a cooling break at relatively low energies, as otherwise the predicted GeV γ-ray spectrum would be too hard to be consistent with the *Fermi*-LAT spectrum.

It is well-known that, due to light-travel-time constraints, the minute-scale variability of blazars like Mrk 501 can not be reproduced with a single-emission-zone model. An interpretation of such extreme variability events might require more complicated geometrical setups, such as the mini-jet-in-jet models of Giannios et al. (2010); Nalewajko et al. (2011). The exploration of such scenarios is outside the scope of this paper. Using our two-zone construction, we therefore focus on the more typical flaring behavior, which is characterized by variability on time scales of $\gtrsim 1$ hour. For a shock speed of $v_{\rm s} = 0.7c$ and a Doppler factor of $\delta = 30$, this yields a characteristic size of the emission zone of $\ell_{\rm rad} = 1.5 \times 10^{15}$ cm, which must correspond to the radiative cooling time of the highest energy electrons in a viable model to reproduce the

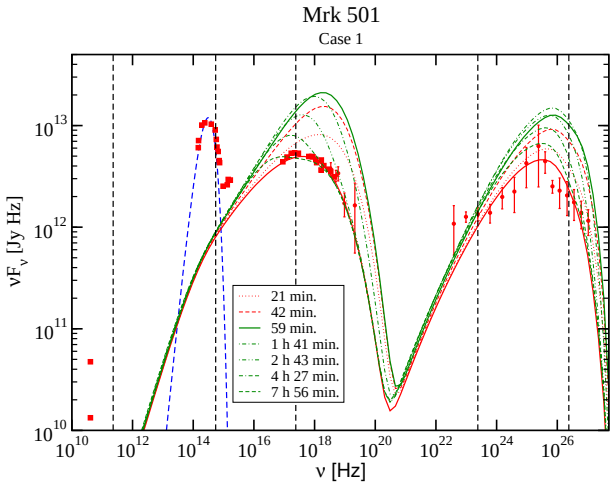


Figure 9. SED of Mrk 501, with data from Abdo et al. (2011). Model curves illustrate the flare simulation for case 1 (variation of only the electron injection luminosity). Red curves indicate model SEDs during the rising, green curves during the decaying part of the flare. The dashed vertical lines indicate the frequencies at which light curves and hardness-intensity diagrams are extracted (see Table 1).

Table 4. Parameters for the quiescent-state model fit to Mrk 501.

Parameter	Value
Electron injection luminosity	$L_{\rm inj,q} = 1.0 \times 10^{39}$ erg s^{-1}
Emission region size	$\ell_{\rm rad} = 1.5 \times 10^{15}$ cm
Jet-frame magnetic field	$B = 0.075$ G
Escape time scale parameter	$\eta_{\rm esc} = 1.0 \times 10^3$
PAS m.f.p. low-energy limit	$\eta_1 = 250$
PAS m.f.p. scaling index	$\alpha = 1.5$
Bulk Lorentz factor	$\Gamma^* \approx \delta = 30$

$\sim 3-6$ hour variability scales. The mean free path $\lambda_{\rm pas}(p) = [m_e c^2/eB]\,\eta_1\,(p/m_e c)^\alpha$ for diffusion of particles for our Monte-Carlo shock acceleration simulation yields a good fit to the Mrk 501 average SED when characterized by $\eta_1 = 250$ and $\alpha = 1.5$. With a magnetic field of $B = 0.075\,{\rm G}$, $m_e c^2/eB = 2.27\times10^4\,{\rm cm}$. Thus, if the characteristic size $\ell_{\rm acc} \equiv \lambda_{\rm pas}(\gamma_{\rm max})$ of the acceleration zone is set equal to $\ell_{\rm rad}$, the confinement constraint leads to a high-energy cut-off in the particle spectrum at $\gamma_{\rm max} = 4.1\times10^5$. In the quiescent-state equilibrium, the magnetization of the emission region is $u_B/u_e = 1.8\times10^{-3}$. The solid red curve in Fig. 9 depicts the resulting quiescent-state SED fit. Note that the optical flux from Mrk 501 appears to be strongly dominated by the contribution of the host galaxy and is unrelated to the jet emission, a common presumption for this source; see, e.g., BBS17 and references therein.

Two generic flaring scenarios are addressed in the following exposition, with parameters summarized in Table 5: (1) A case analogous to the 3C 279 Flare C simulation presented in Section 3.1.1, changing only the electron injection luminosity without modifications of the scattering mean free path parameters, and (2) a case similar to the 3C 279 Flare B simulation of Section 3.1.2, where we also change the pitch angle diffusion parameters to produce a harder electron injection spectrum, in addition to a higher injection luminosity.

Table 5. Flare-state parameters for variability modeling of Mrk 501.

Parameter	Quiescent	Case 1	Case 2
$L_{\rm inj}$ [erg s^{-1}]	1.0×10^{39}	1.0×10^{40}	3.0×10^{39}
η_1	250	250	200
α	1.5	1.5	1.4

3.2.1. *Case 1: Variation of injection luminosity*

In Case 1, we explore a scenario where a strong shock passing through the emission zone enhances only the non-thermal electron injection rate by a factor of 10 to $L_{\rm inj,f} = 1.0\times10^{40}\,{\rm erg\,s^{-1}}$, but leaves the scattering mean free path parameters unchanged. This is analogous to the Flare C simulation for 3C 279 in Section 3.1.1. The resulting snap-shot SEDs are shown in Fig. 9 as red curves during the rising phase of the flare and green curves during the decaying portion, respectively. The heavy solid green curve indicates the peak of the flare, from which one discerns a slight blue-ward shift in the both the synchrotron and SSC peaks; this is caused by progressive acceleration while cooling ensues.

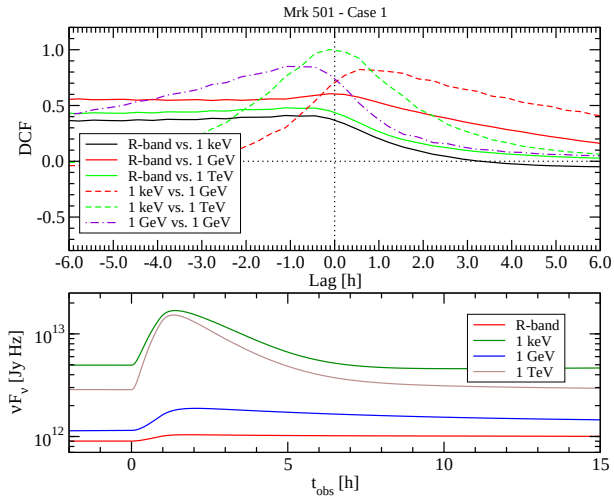


Figure 10. *Bottom:* Multi-wavelength light curves extracted from the case 1 flare simulation for Mrk 501 illustrated in Fig. 9. *Top:* Discrete cross correlation functions evaluated from the case 1 light curves shown in the bottom panel.

Fig. 10 shows the MW light curves for Mrk 501. Obviously, significant TeV γ-ray emission is produced, but the GHz radio band is deep inside the optically-thick part of the synchrotron spectrum, with strongly suppressed flux. The radio light curves are therefore ignored in the following analysis: it is widely presumed that the radio signal emanates from much larger regions of the jet than do the prompt high-energy flares.

Simple scaling arguments based on increases in electron number densities suggest that one would expect an approximately quadratic dependence between the flare amplitudes at the synchrotron and SSC peak frequencies, $\Delta F_{\rm SSC} \propto (\Delta F_{\rm syn})^2$, which is obviously not the case in the SEDs shown in Fig. 9. However, as the light curves in the bottom panel of Fig. 10 illustrate, we find an approximate scaling of $\Delta F_{\rm 1TeV} \propto (\Delta F_{\rm 1keV})^{3/2}$ for the TeV vs. X-ray light curves (note the logarithmic scaling of the flux axis), where the 1 TeV energy is substantially beyond the SSC peak. Comparing multi-GeV energies, an even weaker dependence of the instantaneous flux ratios emerges. This is a result of the time delay due to the gradual build-up of the synchrotron radiation field and the electron population responsible for SSC emission in the GeV band. While the synchrotron flaring amplitude is initially larger than the GeV one, the GeV lightcurve decays much more slowly than the synchrotron one because it is generated by electrons with lower Lorentz

factors. During the late decay phase, several hours after the peak, the GeV γ-ray flux remains elevated far above the quiescent-state level, while the synchrotron flux has essentially decayed back to its quiescent value.

The DCFs in the top panel of Fig. 10 illustrate this point further. While the keV and TeV light curves are tightly correlated with almost zero time lag, the optical and GeV γ-ray light curves are delayed by $\lesssim 0.5$ hrs with respect to the X-ray and TeV light curves, with the long tail towards negative lags resulting from the very slow decay of the optical and GeV light curves. The lag and recovery timescales for this case for Mrk 501 are almost an order of magnitude smaller than those for our Flare C study for 3C 279. This is primarily due to the shorter rise time of the flares in the case of Mrk 501 as a consequence of the smaller emission region (and, thus, shorter shock-crossing time), counteracted by the longer radiative cooling time scales for electrons at the highest energies. The radiative cooling time scale scale is proportional to $\left(B^2\,[1+C]\gamma_{\rm max}\right)^{-1}$, which is ~ 2.2 times larger for Mrk 501 compared to 3C 279 Flare C.

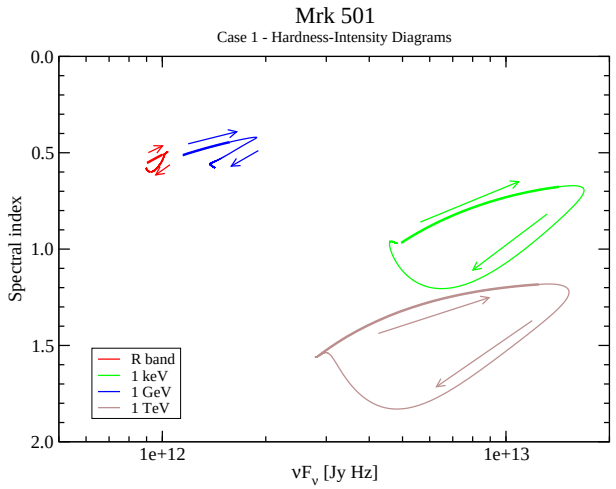


Figure 11. Hardness-intensity diagrams for the case 1 flare simulation for Mrk 501 illustrated in Figs. 9 — 10.

The hardness-intensity diagrams shown in Fig. 11 indicate very pronounced clockwise spectral hysteresis in both the X-ray and TeV γ-ray bands. The large "amplitude" of the hysteresis is a signature of the flux and frequency mobility of the synchrotron and SSC peaks around the chosen frequencies. Such hysteresis has been detected in the case of Mrk 501's "cousin", Mrk 421 (Takahashi et al. 1996). In particular, Figs. 6 and 7 of Tramacere et al. (2009) present HIDs for Swift XRT X-ray observations of 5 flares during the April – July 2006 active period for Mrk 421. The flares were of sub-hour durations. Both clockwise and counter-clockwise hysteresis patterns are present at energies $0.2-10$ keV in the ensemble, and in some cases both directions are realized in a single flare. Fig. 6 of Garson et al. (2010) displays both clockwise and tilted figure-8 hysteresis in $0.5-2$ keV Suzaku data spanning several hours for modest Mrk 421 activity over 4 days in May 2008, a period when the source did not exhibit strong flares. More recently, Figs. 12 and 13 of Abeysekara et al. (2017) display hysteresis profiles for both X-ray and TeV bands on hour-long timescales for two flares in April and May 2014. The HIDs there exhibit clockwise, counter-clockwise and figure-8-like evolution for the hysteresis in both X-ray and VHE γ-ray bands. A similar mix is present in the RXTE data for select flares of Mrk 421 in Fig. 3 of Wang et al. (2018). This presentation of archival RXTE observations of the 5 brightest blazars includes 3 flares from Mrk 501 that also display a mix of hysteresis directions. No clear patterns emerge from this dataset, perhaps the most extensive HID information in the literature for Mrk 501. At much higher energies, the pronounced TeV-band hysteresis predicted by our simulation suggests that its detection should be feasible, at least with the next-generation IACT facility, the Čerenkov Telescope Array (CTA).

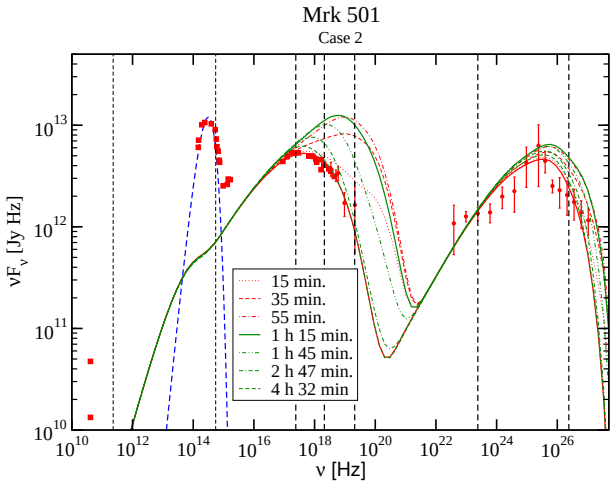


Figure 12. SED of Mrk 501 (data from Abdo et al. 2011) with model curves for case 2 (changing electron luminosity + PAS parameters to produce a harder injection spectrum). Red curves indicate model SEDs during the rising, green curves during the decaying part of the flare. The dashed vertical lines indicate the frequencies at which light curves and hardness-intensity diagrams are extracted (see Table 1); thin lines indicate the radio and optical frequencies which have been ignored in the further analysis.

3.2.2. *Case 2: Variation of $L_{\rm inj}$, η_1, and α*

The spectral variability of Mrk 501 is peculiar in that it sometimes exhibits extreme shifts of the synchrotron (and, to a lesser extend, γ-ray) peak frequency to higher values during flaring states, by more than two orders of magnitude – see, in particular Acciari et al. (2011). Such behavior is obviously not reproduced by our case 1 flare simulations presented above. Therefore, as a second test case, we investigated a scenario in which, in addition to an increased electron injection luminosity, $L_{\rm inj} = 10^{39} \rightarrow 3 \times 10^{39}$ erg s^{-1}, the pitch angle scattering parameters are also changed, specifically $\eta_1 = 250 \rightarrow 200$ and $\alpha = 1.5 \rightarrow 1.4$. This yields a smaller diffusive mean free path $\lambda_{\rm pas}$ for electrons at all energies between thermal and the maximum $\gamma_{\rm max} m_e c^2$, which has the effect of reducing the acceleration time, rendering DSA and SDA more efficient. Physically, this corresponds to somewhat higher levels of MHD turbulence on a range of spatial scales. The resulting evolution of the simulated SEDs is illustrated in Fig. 12. As for case 1, there is no appreciable radio emission from the part of the jet simulated here, and the optical emission is host-galaxy dominated, thus showing negligible variability. Therefore, in the following, both the radio and optical light curves will not be considered.

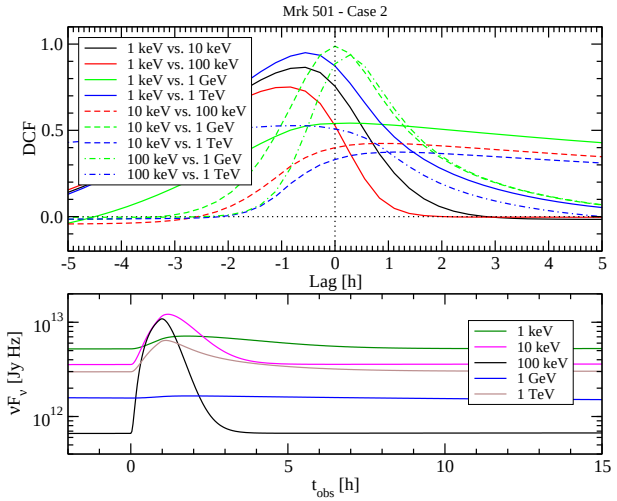


Figure 13. *Bottom:* Multi-wavelength light curves extracted from the case 2 flare simulation for Mrk 501 illustrated in Fig. 12. *Top:* Discrete cross correlation functions evaluated from the case 2 light curves shown in the bottom panel.

The high-frequency synchrotron spectrum predicted by our case 2 simulation shows the expected extreme spectral hardening, with a shift of the synchrotron peak by about a factor of 100, similar to the trend observed in Acciari et al. (2011). This hardening is driven by the greater rapidity of the acceleration, which moves the maximum Lorentz factor in the model up to $\gamma_{\rm max} \approx 1.2 \times 10^6$. Most of the spectral changes occur beyond the quiescent-state synchrotron peak frequency (~ 1 keV), thus resulting in only very moderate variability at 1 keV X-rays. Extreme variations, however, occur in the hard X-ray regime at $\sim 10 - 100$ keV. Therefore, in addition to the standard analysis frequencies used for the previous simulations, we extract light curves and hardness-intensity diagrams at two additional X-ray frequencies, corresponding to 10 keV and 100 keV.

The X-ray (1, 10, and 100 keV) and γ-ray light curves from our case 2 simulation are plotted in the bottom panel of Fig. 13. As expected from the SED evolution (Fig. 12), the variability amplitude is largest at 100 keV and negligible in the *Fermi*-LAT regime (1 GeV). The light curves also suggest time lags within the X-ray bands, with the high-energy variability leading the lower energies.

The decay time scales of the various X-ray light curves in Fig. 13 reflect the energy-dependent radiative (synchrotron + SSC) cooling time scales,

$$t_{\rm cool}^{\rm obs} \approx \frac{0.9}{1+C} \left(\frac{1+z}{\delta} \right)^{1/2} B_{\rm G}^{-3/2} E_{\rm keV}^{-1/2} \ {\rm hr} \approx 4 \, E_{\rm keV}^{-1/2} \ {\rm hr} \quad (8)$$

for the parameters chosen here, where $B_{\rm G} = 0.075$ is the magnetic field in units of Gauss and $C = L_{\rm SSC}/L_{\rm syn}$ (~ 1 for Mrk 501) is the Compton dominance factor, and $E_{\rm keV}$ is the synchrotron photon energy under consideration (Takahashi et al. 1996; Böttcher et al. 2003) in units of keV. This yields $t_{\rm cool}^{\rm obs} \approx 4$ hr for 1 keV and $t_{\rm cool}^{\rm obs} \approx 0.4$ hr for 100 keV. The presence of the expected time lags within the X-ray band is confirmed by the DCFs plotted in the top panel of Fig. 13. However, the lags identified by the DCF are significantly shorter than the differences in cooling time scales, because the DCF peak lags are more strongly dominated by the relative light curve peak times rather than the decay time scales.

As illustrated in Fig. 14, the Case 2 modeling predicts strong spectral hysteresis in the hard X-ray regime (10 keV and 100 keV), with spectral-index variations of $\Delta\Gamma_{\rm ph} \sim 0.7$ between the rising and decaying parts of the flare. A sensitive hard X-ray telescope, such as NuSTAR, should be able to identify such hysteresis patterns. Extensive NuSTAR observations of Mrk 501 do exist (e.g., Pandey et al. 2017; Bhatta et al. 2018). However, while a clear harder-when-brighter trend is clearly seen, e.g., in Fig. 1 of Bhatta et al. (2018), no spectral hys-

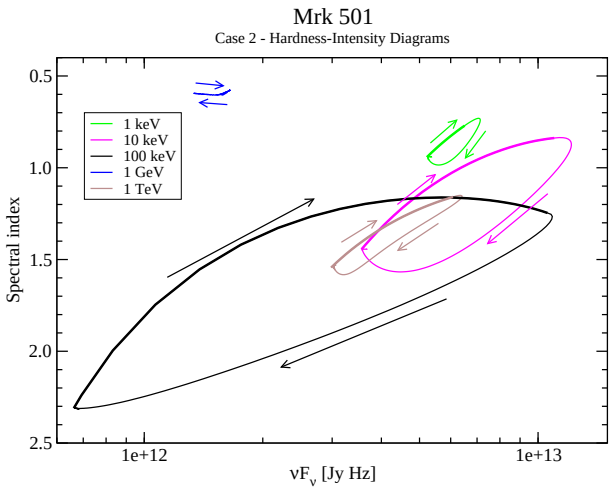


Figure 14. Hardness-intensity diagrams extracted from the case 2 flare simulation for Mrk 501 illustrated in Figs. 12 — 13.

teresis could be clearly identified in the $5-70$ keV window. In our models, modest spectral hysteresis is also predicted at 1 keV and 1 TeV.

4. SUMMARY AND DISCUSSION

We present the development of a numerical scheme to couple Monte-Carlo simulations of diffusive shock acceleration with time-dependent radiation transfer in an internal-shock, leptonic scenario for blazar flares. Our model consists of two zones: A small acceleration zone, in which both DSA and SDA are active, and a larger radiaton zone, into which shock-accelerated electrons are injected in a time-dependent manner. This code has been applied to two prototypical blazars: the FSRQ 3C 279 and the HBL Mrk 501. In both cases, we base our DSA+SDA simulations on a mildly relativistic shock with $v_s = 0.7\,c$ and parameterize the pitch-angle scattering mean-free-path of particles as a power law in particle energy, $\lambda_{\rm pas} = \eta_1\, r_g\, (p/m_e c)^{\alpha-1}$, i.e., $\lambda_{\rm pas} \propto \gamma^\alpha$ at ultra-relativistic energies. As elaborated in our previous work (Baring, Böttcher & Summerlin 2017), producing synchrotron spectra with νF_ν peaks in the optical / infrared (as for low-frequency peaked blazars), requires a strongly electron energy-dependent $\lambda_{\rm pas}$. Specifically, for 3C 279, we obtain a good fit to the average low-state SED using $\eta_1 = 100$ and $\alpha = 3$. For Mrk 501, with an average quiescent-state synchrotron peak at ~ 1 keV, this requirement is relaxed, and a good fit can be obtained with $\eta_1 = 250$ and $\alpha = 1.5$.

Multi-wavelength flares of 3C 279 and Mrk 501 have been simulated by changing the particle acceleration parameters in a time-dependent way. We started our explorations in Section 3.1.1 with Flare C, a somewhat atypical flare of 3C 279 with equal flaring amplitude in the synchrotron and external Compton component. The MW spectrum for this event can be reproduced by simply invoking a higher rate of particle injection, e.g., due to the shock encountering an over-density in the active region of the jet. For this purpose, it has to be postulated that this change in density does not alter the turbulence characteristics on the shock scale in the sense that $\lambda_{\rm pas}(p)$ remains unchanged. The density enhancement would form from MHD substructure on larger, super-parsec scales in the jet, and would not be part of shock-associated turbulence. In such a scenario, the X-ray and radio variability is expected to be delayed with respect to the (simultaneously varying) optical and GeV γ-ray emission by several hours. Moderate spectral hysteresis is predicted for these two bands in our modeling, though this is likely undetectable by current or near-future instrumentation.

An extreme case of an "orphan" γ-ray flare with strongly increasing γ-ray flux and hardening γ-ray spectrum, without an accompanying optical flare, requires more dramatic changes in the jet. This provides a more stringent challenge for our two-zone, acceleration+radiative dissipation modeling. In the framework of leptonic blazar models, such events may be plausibly explained in scenarios where the external target photon field for Compton scattering is temporarily increased, such as the synchrotron mirror models of Böttcher & Dermer (1998); Tavani et al. (2015) or the "Ring of Fire" model of MacDonald et al. (2015, 2017). In this paper, as an alternative scenario, we explored the question whether such flaring behavior can plausibly be reproduced by changing only the particle acceleration characteristics. The harder γ-ray spectrum then required a significantly increased particle acceleration efficiency, implying a smaller $\lambda_{\rm pas}$ at high energies. This can be achieved with smaller values of η_1 and α, indicative of modest increases in turbulence levels in the post-shock region (Summerlin & Baring 2012).

Probes of turbulence changes in blazar shock environs that are independent of this modeling are best acquired through optical polarimetry. Imaging in optical is not possible on the sub-parsec scales of the shocks embedded in jets, but time-dependent measures are. One of the best known examples of this for a blazar is actually for 3C 279, detailed in Abdo et al. (2010b), wherein a dramatic change in optical polarization signatures accompanied a strong "orphan" gamma-ray flare measured by *Fermi*-LAT, beginning on 18th February, 2009 (MJD 54880). Data collected by the Kanata-TRISPEC and La Palma KVA telescopes indicated a gradual change in the polarization angle by 208° that was accompa-

nied by a sharp drop in the V-band polarization degree (PD) from around 35% to around 10%. The polarization degree decline is consistent with an increased level of MHD turbulence on the light-day scales. In our interpretation here, it would signal changing conditions in the pertinent shocked jet region. Directly germane to the Flare B case study here, Figure 7 of Hayashida et al. (2015) exhibits V-band optical polarization data from the Japanese Kanata HOWPol telescope at the level of around 23% just subsequent to Flare B. This would indicate only modest levels of turbulence on 3–5 light-day lengthscales.

In passing, we remark that while the February 2009 flare was almost as strong as our focal 2013 flare, its spectrum in the GeV band was not as flat as that of Flare B. The MW SED exhibited in Figure 2 of Abdo et al. (2010b) suggests that it would probably be well-modeled with similar parameters to our Flare B example, perhaps with slightly lower $\gamma_{\rm max}$, and would also require the choice of a low magnetic field.

An attractive element of our modeling was that the MW spectroscopy and the timescales for Flare B could be accommodated with a single set of system parameters. A notable nuance to this Flare B modeling was that a reduction of the magnetic field was needed in order to compensate the presence of additional high-energy electrons. It is important that after the end of the flaring injection episode, the magnetic field was required to gradually relax back to restore its higher quiescent-state level to compensate for the gradual cooling of the additionally injected high-energy electrons. A key question concerns whether such prompt but ephemeral reductions are realistic. While MHD simulations of jets typically only indicate magnetic fluctuations in $|\mathbf{B}|$ by factors of $2-3$, they cannot resolve structures on the subparsec scales pertinent to this question. Interestingly, kinetic plasma PIC simulations of relativistic shocks do see strong magnetic field strength contrasts, by factors of $10-20$ in Weibel-instability-generated turbulence (e.g., Sironi, Spitkovsky & Arons 2013). However, these variations are on the extremely small inertial scales $c/\omega_p \sim 10^3 - 10^6$ cm that are not germane to the high energy electrons that emit optical synchrotron and inverse Compton gamma-rays.

Yet it is interesting to note that magnetometer measurements of active regions just downstream of nonrelativistic interplanetary shocks in the solar wind do exhibit sharp magnetic rarefactions, albeit by factors of around $1.5-2$ in field strength (e.g., see Ulysses B-field data streams in Baring et al. 1997), followed by some recovery. The magnetic field in these heliospheric rarefactions also changes direction, perhaps in a manner broadly consistent with what is invoked to explain the 3C 279 polarization angle swing highlighted in Abdo et al. (2010b). On the basis of these varied pieces of information, it appears that our choice of a reduction in $|\mathbf{B}|$ by around a factor of 9 is not particularly concerning, though it is difficult to draw tight conclusions pertaining to its appropriateness without further observational information. Results from a future gamma-ray polarimeter, such as the planned AMEGO[2] and e-ASTROGAM (see De Angelis et al. 2017) missions, could well enlighten the picture.

For Mrk 501 we also started with a simple scenario of increasing the number of injected electrons without changing the turbulence characteristics, i.e., leaving $\lambda_{\rm pas}(\gamma)$ unchanged. Such a scenario leads to correlated variability across the electromagnetic spectrum (except for the optical, which is host-galaxy dominated), with the GeV γ-ray flux variations lagging behind the simultaneously-varying keV X-ray and TeV fluxes by $\sim$ 1 hour. Significant spectral hysteresis in the X-ray and TeV bands was predicted.

Mrk 501 sometimes exhibits a significant shift of the synchrotron peak frequency to higher values during flaring states (e.g., Acciari et al. 2011). In order to reproduce such a scenario, we ran a second simulation, invoking an increased particle acceleration efficiency through a decreasing $\lambda_{\rm pas}$ at high energies (changing $\eta_1 = 250 \rightarrow 200$ and $\alpha = 1.5 \rightarrow 1.4$). Such changes could be indicative of modest increases in turbulence levels in the post-shock region. This case study approximately reproduces the significant synchrotron peak shift observed by Acciari et al. (2011), and predicts strong hard X-ray spectral hysteresis, potentially detectable by NuSTAR, and time lags between different X-ray energy ranges (1 – 100 keV) of the order of $\lesssim 1$ hour. Importantly, the time lags identified by the discrete correlation function are significantly shorter than the differences in radiative cooling time scales, which govern primarily the decay time scales of flares at different energies. Several authors (e.g., Takahashi et al. 1996; Böttcher et al. 2003) have suggested that measured inter-band time lags can be used to estimate the strength of the magnetic field under the assumption that these time lags reflect differences in the radiative cooling time scales. Our study illustrates that this protocol is at risk of under-estimating the actual radiative cooling time scales and, thus, overestimate the magnetic field by a factor of a few. Careful investigation via temporal correlation functions can ameliorate this complication.

[2] see `https://asd.gsfc.nasa.gov/amego/index.html`.

This fairly diverse selection of flare case studies clearly highlights the broad viability of our approach of combining particle acceleration and MW emission simulations in a two-zone construction to modeling quiescent and flaring phases of the blazars 3C 279 and Mrk 501. Moreover, it illustrates the richness in time dependent information delivered by such an integrated theory analysis, motivating more intensive observational scrutiny by multi-wavelength campaigns during active phases of bright blazars. We anticipate that during the CTA era, it will prove possible to perform incisive diagnostics into the competition between acceleration and radiative cooling that have a broader scope than just probing simple temporal injection profiles $Q_e(\gamma_e, t)$ like those employed in this investigation.

ACKNOWLEDGMENTS

We thank the anonymous referee and Anita Reimer for suggestions helping to improve the presentation. The work of M. Böttcher is supported by the South African Research Chairs Initiative (grant no. 64789) of the Department of Science and Innovation and the National Research Foundation[3] of South Africa. MGB and MB are grateful to NASA for partial support for early parts of this research program through the Astrophysics Theory Program, grant NNX10AC79G. MGB is also grateful for support from the NASA *Fermi* Guest Investigator Program through grant 80NSSC18K1711.

REFERENCES

Abdo, A. A., Ackerman, M., Ajello, M., et al., 2010, ApJ, 715, 429.

Abdo, A. A., Ackermann, M., Ajello, M., et al. 2010, Nature, 463, 919.

Abdo, A. A., et al., 2011, ApJ, 727, 129.

Abeysekara, A. U., Archambault, S., Archer, A., et al. 2017, ApJ, 834, 2.

Acciari, V. A., et al., 2011, ApJ, 729, 2.

Ahnen, M. L., et al., 2018, A&A, 620, A181.

Albert, J., et al., 2007, ApJ, 669, 862.

Baring, M. G., Böttcher, M. & Summerlin, E. J., 2017, MNRAS, 464, 4875. [BBS17]

Baring, M. G., W. Ogilvie, C. Ellison, et al. 1997, ApJ, 476, 889.

Barniol Duran, R., Tchekhovskoy, A., & Giannios, D. 2017, MNRAS, 469, 4957.

Bhatta, G., Mohorian, M., & Bilinsky, I., 2018, A&A, 619, A93.

Böttcher, M. & Baring, M. G., 2019, in Proc. of "High Energy Astrophysics in Southern Africa 2018" (HEASA 2018), PoS(HEASA2018), in press (arXiv:1903.12381).

Böttcher, M., Basu, S., Joshi, M., et al. 2007, ApJ, 670, 968.

Böttcher, M., Mause, H., & Schlickeiser, R., 1997, A&A, 324, 395.

Böttcher, M. & Dermer, C. D., 1998, ApJ, 501, L51.

Böttcher, M. & Chiang, J., ApJ, 2002, 581, 127.

Böttcher, M., Marscher, A. P., Ravasio, M., et al., 2003, ApJ, 596, 847.

Böttcher, M., Reimer, A., & Marscher, A. P., 2009, ApJ, 703, 1168.

Böttcher, M. & Dermer, C. D., 2010, ApJ, 711, 445.

Böttcher, M., Reimer, A., Sweeney, K. & Prakash, A., ApJ, 2013, 768, 54.

Bradbury, S. M., et al., 1997, A&A, 320, L5.

Catanese, M., et al., 1997, AIP Conf. Proc., 410, 1402.

Cerutti, B., Uzdensky, D. A. & Begelman, M. C., ApJ 2012, 746, 148.

Chen, X., Fossati, G., Liang, E. P., & Böttcher, M., 2011, MNRAS, 416, 2368.

Chen, X., Fossati, G., Böttcher, M., & Liang, E. P., 2012, MNRAS, 424, 789.

Crumley, P., Caprioli, D., Markoff, S., et al. 2019, MNRAS, 485, 5105

De Angelis, A., Tatischeff, V., Tavani, M., et al. 2017, Experimental Astronomy, 44, 25.

Decker, R. B., & Vlahos, L. 1986, ApJ, 306, 710

De Naurois, M., 2018, Astronomer's Telegram # 11680.

Dondi, L. & Ghisellini, G., MNRAS, 1995, 273, 583.

Edelson, R. A., & Krolik, J. H., 1988, ApJ, 333, 646.

Ellison, D. C. & Double, G. P., 2004, Astropart. Phys., 22, 323.

Ellison, D. C., Jones, F. C. & Reynolds, S. P., 1990, ApJ, 360, 702.

Finke, J. D., Razzaque, S., & Dermer, C. D., 2010, ApJ, 712, 238.

Garson, A. B., Baring, M. G., & Krawczynski, H. 2010, ApJ, 722, 358.

Ghisellini, G., Padovani, P., Celotti, A., et al. 1993, ApJ, 407, 65.

Ghisellini, G., Tavecchio, F., Foschini, L., Ghirlanda, G., Maraschi, L., & Celotti, A., 2010, MNRAS, 402, 497.

Giannios, D., Uzdensky, D., & Begelman, M. C., 2010, MNRAS, 402, 1649.
Graff, P. B., Georganopoulos, M., Perlman, E. S., & Kazanas, D., 2008, ApJ, 689, 68.
Grazian, A., Cristiani, S., D'Odorico, V., Omizzolo, A., & Pizzella, A., 2000, AJ, 119, 2540.
Hartman, R. C., et al., 2001, ApJ, 553, 683.
Hayashida, M., et al., 2015, ApJ, 807, 79.
Inoue, S. & Takahara, F., ApJ, 1996, 463, 555.
Jorstad, S. G., Marscher, A. P., Lister, M. L., et al., 2005, AJ, **130**, 1418.
Joshi, M., & Böttcher, M., 2011, ApJ, 727, 21.
Kirk, J. G. & Heavens, A. F., 1989, MNRAS, 239, 995.
Kirk, J. G., Rieger, F. M., & Mastichiadis, A. 1998, A&A, 333, 452.
Lynds, C. R., Stockton, A. N., & Livingston, W. C., 1965, ApJ, 142, 1667.
MacDonald, N. R., Marscher, A. P., & Jorstad, S. G., 2015, ApJ, 804, 111.
MacDonald, N. R., Jorstad, S. G., & Marscher, A. P., 2017, ApJ, 850, 87.
Maraschi, L., Ghisellini, G., & Celotti, A. 1992, ApJ, 397, L5.
Marcowith, A., Bret, A., Bykov, A., et al. 2016, Reports on Progress in Physics, 79, 046901
Marscher, A. P., & Gear, W. K., 1985, ApJ, 298, 114.
Meliani, Z., Keppens, R., & Giacomazzo, B. 2008, A&A, 491, 321.
Mimica, P., Aloy, M. A., Müller, E., & Brinkmann, W., 20094, A&A, 418, 947.
Nalewajko, K., Giannios, D., Begelman, M. C., Uzdensky, D. A., & Sikora, M., 2011, MNRAS, 413, 333.
Pandey, A., Gupta, A. C., & Wiita, P. J., 2017, ApJ, 841, 123.
Petry, D., et al., 2000, ApJ, 536, 742.
Porth, O. 2013, MNRAS, 429, 2482.
Quinn, J., et al., 1996, ApJ, 456, L83.
Sironi, L., & Spitkovsky, A. 2009, ApJ, 707, L92.
Sironi, L., & Spitkovsky, A. 2014, ApJL, 783, L21
Sironi, L., Spitkovsky, A., & Arons, J. 2013, ApJ, 771, 54.
Sokolov, A., Marscher, A. P., & McHardy, I. M., 2004, ApJ, 613, 725.
Sokolov, A., & Marscher, A. P., 2005, ApJ, 625, 52.
Spada, M., Ghisellini, G., Lazzati, D., & Celotti, A., 2001, MNRAS, 325, 1559.
Stecker, F. W., Baring, M. G., & Summerlin, E. J. 2007, ApJL, 667, L29
Summerlin, E. J. & Baring, M. G., 2012, ApJ, 745, 63.
Takahashi, t., et al., 1996, ApJ, 470, L89.
Tavani, M., Vittorini, V., & Cavaliere, A., 2015, ApJ, 814, 51.
Teshima, M., et al., 2008, in proc. of 30th ICRC, Eds. Caballero, R., D'Olivo, J. C., Medina-Tanco, G., Nellen, L., Sánchez, F. A. & Valdés-Galicia, J. F., Mexico City, Mexico, vol. 3, p 1045.
Tramacere, A., Giommi, P., Perri, M., et al. 2009, A&A, 501, 879.
Wang, Y., Xue, Y., Zhu, S., et al. 2018, ApJ, 867, 68.
Wehrle, A. E., et al., 1998, ApJ, 497, 178.
Yan, D., Zhang, L., & Zhang, S.-N. 2016, MNRAS, 459, 3175.